Multivalent-Ion versus Proton Insertion into Nanostructured Electrochromic WO3 from Mild Aqueous Electrolytes

Tom Rocca, Ari Gurel, Delphine Schaming, Benoît Limoges, Véronique Balland

Multivalent-ion versus proton insertion

into nanostructured electrochromic WO_3 from mild aqueous electrolytes

T. Rocca,[1] A. Gurel,[2] D. Schaming,[2] B. Limoges,[1,*] V. Balland[1,*]

1- Université Paris Cité, Laboratoire d'Electrochimie Moléculaire, UMR 7591, 75006 Paris Cedex 05
2- Université Paris Cité, ITODYS, UMR 7086, 75006 Paris Cedex 05

Corresponding authors:

limoges@u-paris.fr

veronique.balland@u-paris.fr

Keywords

Aqueous battery, smart window, proton insertion, spectroelectrochemistry, tungsten oxide

Abstract

Mild aqueous electrolytes containing multivalent metal salts are currently scrutinized for the development of eco-sustainable energy-related devices. However, the role of soluble multivalent metal ions in the electrochemical reactivity of transition metal oxides is a matter of debate, especially when performed in protic aqueous electrolytes. Here, we have compared, by means of (spectro)electrochemistry, the reversible electrochromic reduction of transparent nanostructured γ-WO_3 thin films in mild aqueous electrolytes of various chemical composition and pH. This study reveals that reversible proton-insertion is the only charge storage mechanism over a large pH-range, and that it is effective for aqueous electrolytes prepared from either organic (such as acetic acid) or inorganic (such as solvated multivalent cations) Brønsted acids. By refuting charge storage mechanisms relying on the reversible insertion of multivalent metal ions, notably in aqueous electrolytes based on Al^{3+} ions or a mixture of Al^{3+} and Zn^{2+} ions, these fundamental results pave the way for the rational development of electrolytes and active materials for a range of aqueous-based devices, such as the emerging concept of energy-saving smart window which we also address in this study.

Introduction

Tungsten oxide (WO_3) is an earth-abundant and versatile transparent n-type semiconductor of great interest for a broad range of applications.[1] Its ability to reversibly insert small cations during electrochemical reduction is at the origin of its electrochromic properties, which have been successfully exploited up to the commercialisation of energy-saving smart windows.[2,3] This intercalation property also confers charge storage properties,[4] which, combined with electrochromic properties, have led to the emergence of the concept of bi-functional electrochromic charge-storage devices.[5–7] WO_3 is also used for other energy-related applications, including solar-driven photoelectrochemical conversion thanks to the combination of transparency and semiconductive properties.[8]

Many of the above-mentioned applications rely on the use of aqueous electrolytes, which have the merit of combining several advantages such as high ionic conductivity, non-toxicity, and eco-sustainability. It is therefore essential to understand the electrochemical reactivity of WO_3 in aqueous electrolytes, especially as these protic media are well known to engender proton-coupled electron transfer (PCET) processes. This is clearly the case in strongly acidic aqueous electrolytes (typically containing H_2SO_4), where it has been unambiguously established that WO_3 can reversibly reduce to a H_xWO_3 bronze phase according to the following electrochemical reaction:[9]

$$\mathrm{WO_3} + x\,\mathrm{H^+} + x\,\mathrm{e^-} \rightleftarrows \mathrm{H_xWO_3} \qquad (1)$$

This proton-insertion coupled electron transfer (PICET) reaction characterises the reactivity of WO_3 not only in terms of faradaic charge storage[10,11] and electrochromism[12,13] but also in terms of hydrogen evolution as the later has recently been proposed to be linked to the bulk intercalation of protons.[14,15]

However, reversible proton insertion in WO_3 is usually achieved from strongly acidic aqueous electrolytes, which results in WO_3 degradation due to dissolution and redeposition side reactions.[16,17] Therefore, optimizing the electrolyte to operate under less acidic and corrosive conditions, typically in the 2-3 pH range to mitigate chemical dissolution/corrosion of WO_3,[18] is a route to improve the stability and cyclability of WO_3 films. At the same time, it is advisable to favour nanoporous and even amorphous WO_3 films as it reduces the average insertion distance of cations within the solid phase, and also to prefer small size charge carriers as they are expected to lead in high rate capabilities and fast colour switching times through fast solid-state diffusion.[19] For these reasons, several groups have explored the possibility of reversibly inserting small multivalent cations such as Al^{3+} and/or Zn^{2+} into WO_3, using multivalent ions-based weakly acidic aqueous electrolytes.[6,20–30] In these works, the reversible insertion of Al^{3+} was finally asserted as the effective

electrochromic charge storage mechanism for monoclinic $W_{18}O_{49}$ nanowires,[20–23] nanostructured hexagonal WO_3,[24,25] amorphous WO_3,[26,6,27] nanosheets WO_3,[28] but also for mixed oxides such as $Nb_{18}W_{16}O_{93}$.[29] A recurrent argument to support this intercalation mechanism is that Al^{3+} has a smaller ionic radius (54 pm) than Li^+ (76 pm). However, this simplistic view ignores the high migration barrier that the highly positively charged Al^{3+} cation must overcome to insert and diffuse within the metal oxide structure.[31] It also does not take into account the fact that, in aqueous media, Al^{3+} is strongly solvated by water, forming a large size hexaaqua metal ion complex (*i.e.*, $[Al(H_2O)_6]^{3+}$) associated to a high solvation energy.[32] This complex is also known for its weak Brønsted acid properties,[33] and can therefore provide protons as solid-state charge carriers, as previously demonstrated by us for TiO_2 or MnO_2.[34,35]This is also what has prompted J. Guoto *et al.* to propose that in a hybrid-cation $AlCl_3{\cdot}6H_2O$ 1,2-propylene glycol electrolyte, the electrochromic properties of an amorphous WO_{3-x} film are mainly linked to the reversible insertion of protons with concomitant formation of an aluminium-hydroxide-based solid electrolyte interphase.[36] This work therefore runs counter to the previous works proposing the insertion of Al^{3+} into a WO_3 material when operating in an Al^{3+}-based electrolyte. Herein, we examine the electrochemical reactivity of a nanostructured crystalline WO_3 film in a range of mild-aqueous electrolytes, including Al^{3+}-based and Zn^{2+}-based aqueous electrolytes, with the aim to unambiguously reveal the chemical nature of the solid-state charge carrier reversibly inserting in WO_3 and providing its electrochromic charge storage properties. This is an essential question to answer,[37] in order to rationalise and improve the functioning of WO_3-based electrochromic devices. So, in this work we address this question for nanostructured γ-WO_3 electrodes in both the configuration of a conventional 3-electrode set-up and that of a 2-electrode smart window device.

Results and discussion

WO_3 Electrodes. Nanostructured γ-WO_3 films were prepared on transparent FTO-coated glass electrodes by a hydrothermal method (see Experimental Section for details). The areal amount of active material was typically 0.05-0.1 mg/cm^2, with a thickness ranging from 300 to 400 nm. The monoclinic structure of the pristine porous material was confirmed by XRD (see Figure 1B) with three main peaks observed at 2θ = 26.9, 27.5 and 28.3°, corresponding respectively to (002), (020) and (200) crystal planes (ICDD file 43-1035). From XRD, the crystallite size was estimated to 50 nm $\times$ 106 nm, while the SEM images confirmed the high porosity of the thin film (Figure 1A).

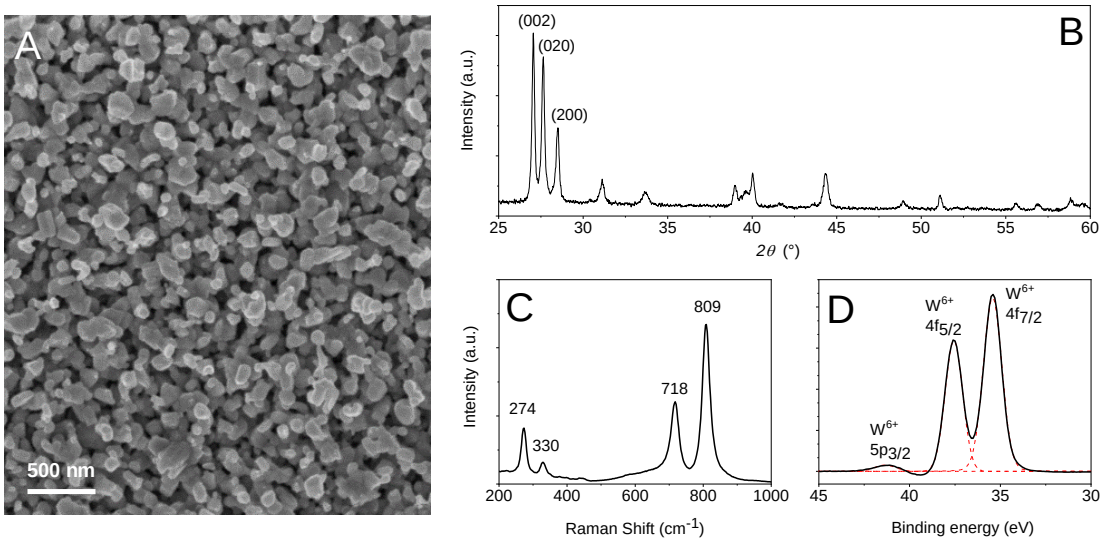

Figure 1. (A) Scanning electron microscope image of the WO_3 thin film. (B) X-Ray diffractogram of the WO_3 thin film. (C) Raman spectrum of the material. (D) Extract of the XPS spectrum of the synthesized WO_3 thin film.

The Raman spectrum (Figure 1C) showed the two characteristic O-W-O stretching bands at 718 and 809 cm^{-1}, specific to the monoclinic structure,[38] as well as two O-W-O bending bands in the 260-340 cm^{-1}. The XPS core-level W spectrum of the film was deconvoluted into three peaks (Figure 1D). The two main peaks at 35.4 and 37.6 eV were attributed to W $4f_{7/2}$ and W $4f_{5/2}$ of the W^{6+} oxidation state, confirming the fully oxidized state of the pristine WO_3 film. A weak emission peak originating from the W $5p_{3/2}$ is also observed at 41.1 eV. This confirms the formation of non-defective WO_3, without significant oxygen vacancies.

Electrochemical characterisation. The nanostructured WO_3 electrodes were first investigated by cyclic voltammetry in a 3-electrode cell configuration, with a degassed aqueous electrolyte. The latter was either a 0.1 M H_2SO_4 solution of pH 0.95 (containing thus ~ 0.1 M H_3O^+) or a 0.5 M acetate buffer of pH 4.6 (containing 0.25 M acetic acid, 0.25 M acetate, and ~ 10^{-5} M H_3O^+, along with 0.5 M KCl to maintain a high and almost constant ionic strength). The cyclic voltammograms (CVs) recorded at 5 mV/s in these two electrolytes are shown in Figure 2A, with the scanned potential window adjusted by -60 mV/pH unit to account for the potential shift of the pH-dependent faradaic waves. Their overall shape is very similar in both electrolytes, showing two clearly well-defined reduction peaks of almost identical magnitude, and a single reoxidation peak of lesser amplitude, broader and less defined. These features are also common to those previously reported for monoclinic WO_3 nanoparticle-based electrodes (either based on nanostructured films or composite electrode materials) in acidic electrolytes.[10,13,39–41] From peaks integration, the overall charge passed during the reductive scan at 5 mV/s is 38 mA·h/g in both electrolytes, while the Coulombic efficiency (CE)

after a complete cycle is 95% and 83% in the acidic and buffered electrolyte, respectively. These moderate CE values can be attributed to a lack of reversibility in proton insertion, as evidenced by the residual blue coloration of the electrode at the end of the CV. This incomplete reversibility has already been reported for nanoparticulate monoclinic WO_3 films and attributed to "stranded" hydrogen atom isolated in the semiconductive WO_3 matrix, thereby requiring a large overpotential to be completely disinserted.[41] This difficulty in extracting protons also seems to correlate in CV with the slow, broad and ill-defined reoxidation wave. Accordingly, a resting potential of + 0.7 V was systematically applied for a few minutes (> 5 min) at the end of each CV to ensure complete reoxidation of the metal oxide film and hence full recovery of the electrode's transparency. Thanks to this procedure, the CVs recorded successively at the same electrode are superimposed (Figure S1), attesting to the recovery of the same initial state after each CV.

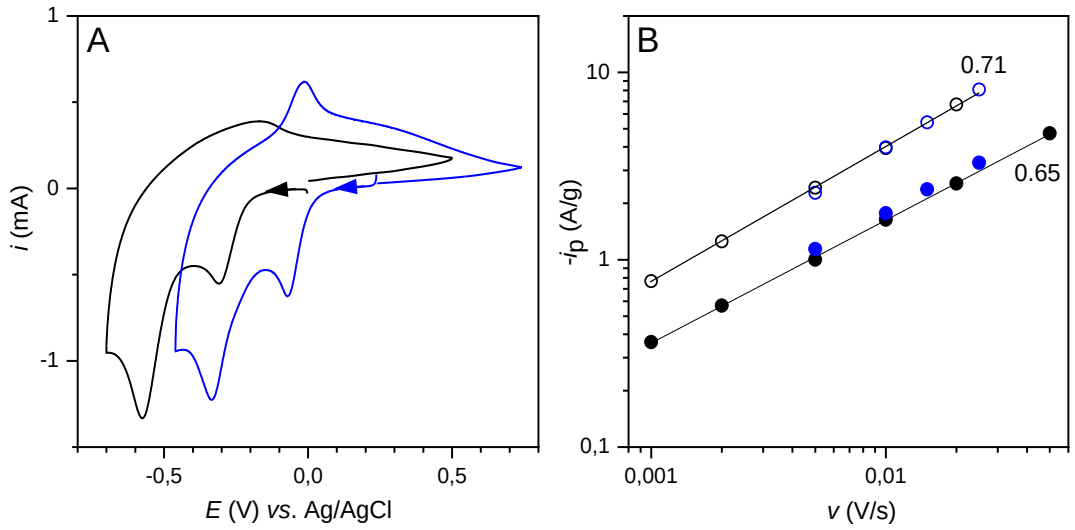

Figure 2. (A) CVs recorded at 5 mV/s at the WO_3 electrode in (blue) 0.1 M H_2SO_4 of pH 0.95 and (black) 0.5 M acetate buffer of pH 4.6 (along with 0.5 M KCl). (B) Scan rate-dependence of the (solid dots) first and (empty dots) second cathodic peak potential, with identical colour code as in (A).

At 5 mV/s, the potential of each cathodic peak is shifted by -0.24 V between the acid and buffered electrolytes, indicating different thermodynamics of the faradic processes in each electrolyte. This potential shift is close to the theoretical value of -0.22 V expected for a proton-coupled electron transfer reaction involving an identical number of protons and electrons and for a pH rising from 0.95 to 4.6. CVs were next recorded at different scan rates (Figure S2). At 1 mV/s, a maximum gravimetric capacity of 58 mA·h/g with a CE of 96% was achieved after a complete cycle in the acetate buffer (Figure S2), indicating the reversible insertion of x = 0.5 protons per WO_3. In the log-log plot of Figure 2B, intensities of both cathodic peaks scale linearly with the scan rate, with slopes of close values (0.65 and 0.71). These values comprised between 1 and 0.5 indicate that the faradaic processes are halfway between a surface-controlled reaction and a diffusion-controlled process, and this whatever

the nature and pH of the electrolyte. As a result, we can conclude on a common reversible PICET mechanism in the nanostructured WO_3 film. The inserted protons are assumed to be provided by the AH Brønsted acids present in the electrolytes, which can thus be either H_3O^+ (pK_a = 0) in H_2SO_4 or CH_3COOH (pK_a = 4.7) in the acetate buffer, leading finally the following global electrochemical reaction:

$$WO_3 + x\ e^- + x\ AH \rightleftarrows H_xWO_3 + x\ A^- \qquad (2)$$

where A^- stands for the conjugated base of the Brønsted acid (*i.e.* H_2O in H_2SO_4 or CH_3COO^- in the acetate buffer).

We next repeated the experiment in different buffered electrolytes ranging from phosphate buffer at pH 6.95 to ammonia buffer at pH 9.5 (see Experimental Section). As shown in Figure 3A, the CVs share common characteristics over the entire pH range investigated, with two well-defined faradaic reduction peaks and a single reoxidation wave, more or less broad.

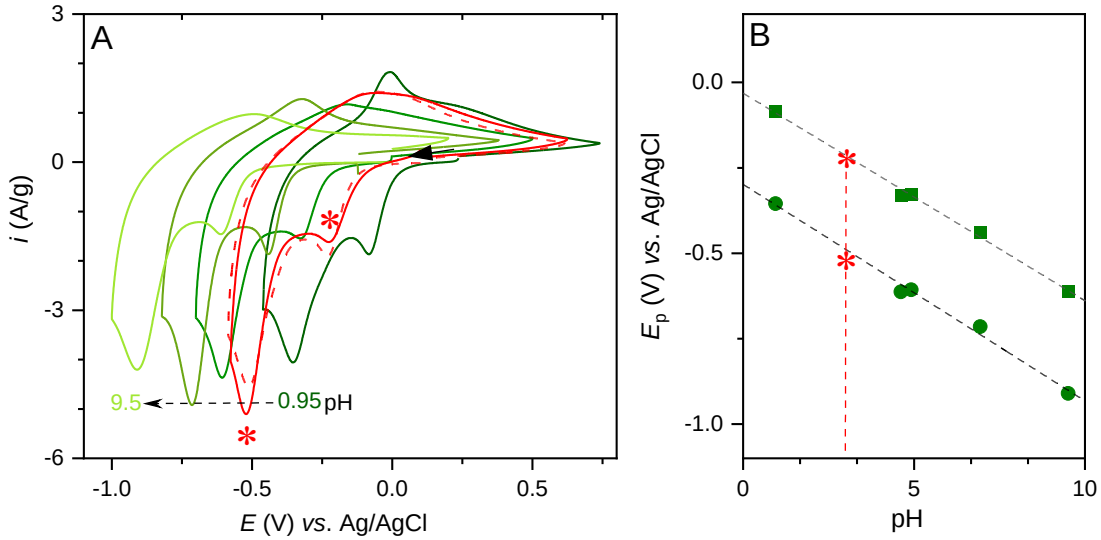

Figure 3. (A) CVs recorded at 10 mV/s at the WO_3 electrode in a range of (green) buffered and (red) unbuffered aqueous electrolytes ranging from pH 0.95 to 9.5. The plain and dashed red CVs were recorded, respectively, in an unbuffered 0.25 M $AlCl_3$ electrolyte (pH 3) and in an unbuffered 0.25 M acetic acid (along with 0.5 M KCl). (B) pH-dependence of the (squares) first and (dots) second reduction peak potential. The green dashed lines are the corresponding linear regressions with slopes of -61 and -63 mV/pH unit, respectively. The red stars correspond to the reduction peak potentials recorded in the 0.25 M $AlCl_3$ electrolyte.

The potential positions of the two reduction peaks are clearly pH-dependent, with slopes close to -59 mV/pH unit (Figure 3B). Such pH dependency had already been reported for H_xWO_3 bronzes ($0.004 < x < 0.1$) in H_2SO_4 electrolytes of pH ranging from 0.9 to 2.3.[42] Here, we demonstrate that it extends over a wider pH range and also remains valid for the second reduction peak. This pH dependence suggests that each reduction peak corresponds to a proton-coupled electron transfer reaction, in which an identical number of protons and electrons are involved. This unambiguously demonstrates

that the proton is the solid-state charge carrier that compensates for the negative charge injected into WO_3 upon reduction, irrespective of the chemical nature of the weak Brønsted acid (*i.e.*, acetic acid, phosphate, or ammonium) and conjugated base present in the electrolyte. In addition, this demonstrates that the potassium cation that has been sometimes deliberately added to the electrolyte to improve the ionic conductivity is not involved in the charge storage mechanism. Accordingly, we can conclude that the faradaic charge storage mechanism of WO_3 exclusively relies on eq. 2 over a wide range of pHs. However, it should be noted that this equation is somewhat simplistic, as it fails to reflect the passage through different stable reduced structures of H_xWO_3 as a function of the applied potential, as it has been proposed in some previous works.[11,41]

Next, the electrode was cycled in an unbuffered aqueous electrolyte containing 0.25 M $AlCl_3$. Upon dissolution of the $AlCl_3$ salt in water, the Al^{3+} cation is rapidly converted to a weak acidic hexaaqua $[Al(H_2O)_6]^{3+}$ complex,[43] which acidity is governed by the following acid-base equilibrium (or protolysis reaction) and the associated thermodynamic equilibrium constant K_a :

$$[\mathrm{Al(H_2O)_6}]^{3+} + \mathrm{H_2O} \rightleftharpoons [\mathrm{Al(H_2O)_5(OH)}]^{2+} + \mathrm{H_3O^+} \qquad (3)$$

With a pK_a of 5,[33] a bulk pH of 3 is thus obtained for a 0.25 M $AlCl_3$ solution. The CV of WO_3 in this electrolyte leads to a behavior very similar (red curve in Figure 3A) to that recorded in buffered aqueous electrolytes. Furthermore, the reduction peaks are positioned at values that correspond to those expected for an aqueous electrolyte at pH 3, aligning well with the pH-dependent straight lines in Figure 3B (red solid stars), which therefore suggests that we are dealing with a PICET charge storage mechanism. To confirm this assumption, the electrode was then cycled in an unbuffered electrolyte of pH 3 containing 0.25 M acetic acid, a weak Brønsted organic acid whose pK_a of 4.76 [44] is very close to that of $[Al(H_2O)_6]^{3+}$. Figure 3A shows that the CV recorded in this unbuffered electrolyte (dashed red line) almost overlaps the one recorded in the Al^{3+}-based electrolyte at a same pH. This overlap of the two voltammograms clearly reflects a faradic charge storage mechanism characterized by identical kinetics and thermodynamics in both electrolytes, making thus a strong argument in favour of a PICET mechanism. In the Al^{3+}-based electrolyte, we assume that $[Al(H_2O)_6]^{3+}$ acts as a proton donor at the metal oxide/electrolyte interface, according to the following electrochemical reaction:[34,35]

$$\mathrm{WO_3} + x\ \mathrm{e^-} + x\ [\mathrm{Al(H_2O)_6}]^{3+} \rightleftharpoons \mathrm{H_xWO_3} + x\ [\mathrm{Al(H_2O)_5(OH)}]^{2+} \qquad (4)$$

Note that while the potential of the first reduction peak recorded in Al^{3+}- or acetic acid-based electrolytes is fully in line with what we would expect for a pH 3 aqueous electrolyte, the potential of the second reduction peak is slightly shifted towards a more negative value than expected (see red solid stars in Fig. 3B). This behaviour is in reality fully consistent with the fact that the $AlCl_3$ and acetic

acid electrolytes are not buffered, so that the insertion of protons leads to a significant local increase in pH at the electrode/electrolyte interface, and consequently to a shift in the proton-coupled reduction peak potential according to the Nernst equation.[45]

Smart window assembly. As WO_3 is an electrode material widely used in the design of electrochromic devices, we decided to extend this work by studying the spectroelectrochemistry of WO_3 in the context of a two-electrode smart window. For this purpose, we have chosen to take advantage of a zinc frame as the counter electrode (*i.e.*, anode), the latter having recently reported to be particularly useful for developing a new concept of energy-saving Zn-based smart windows.[6] In order to ensure the efficient reversible electrodeposition of zinc metal at the anode, the aqueous electrolyte has to contain a certain amount of Zn^{2+} ions, which may thus contribute to the reversible charge storage mechanism. Indeed, it may either be itself an inserting charge compensating cation,[46] or a proton supplier on account of the weak Brønsted acidity of its solvated hexaaqua complex (pK_a of 9.0).[33] This thus calls for a rigorous study to unambiguously identify the chemical nature of the solid-state charge carrier under conditions where Zn^{2+} is present in the electrolyte.

To this end, we constructed a 2.5 x 2.5 cm^2 smart window by combining a transparent WO_3 electrode with a zinc metal frame and a microscope slide as the rear window, each separated by a silicone frame (see Fig 4D and Experimental Section for details). The device was filled with a degassed aqueous electrolyte of pH 3, containing 0.1 M of $ZnCl_2$ and either 0.25 M $AlCl_3$, 0.25 M acetic acid, or 1 M KCl. The device was then characterized by cyclic voltammetry while simultaneously recording the transmittance. The experimental data are gathered in Figure 4.

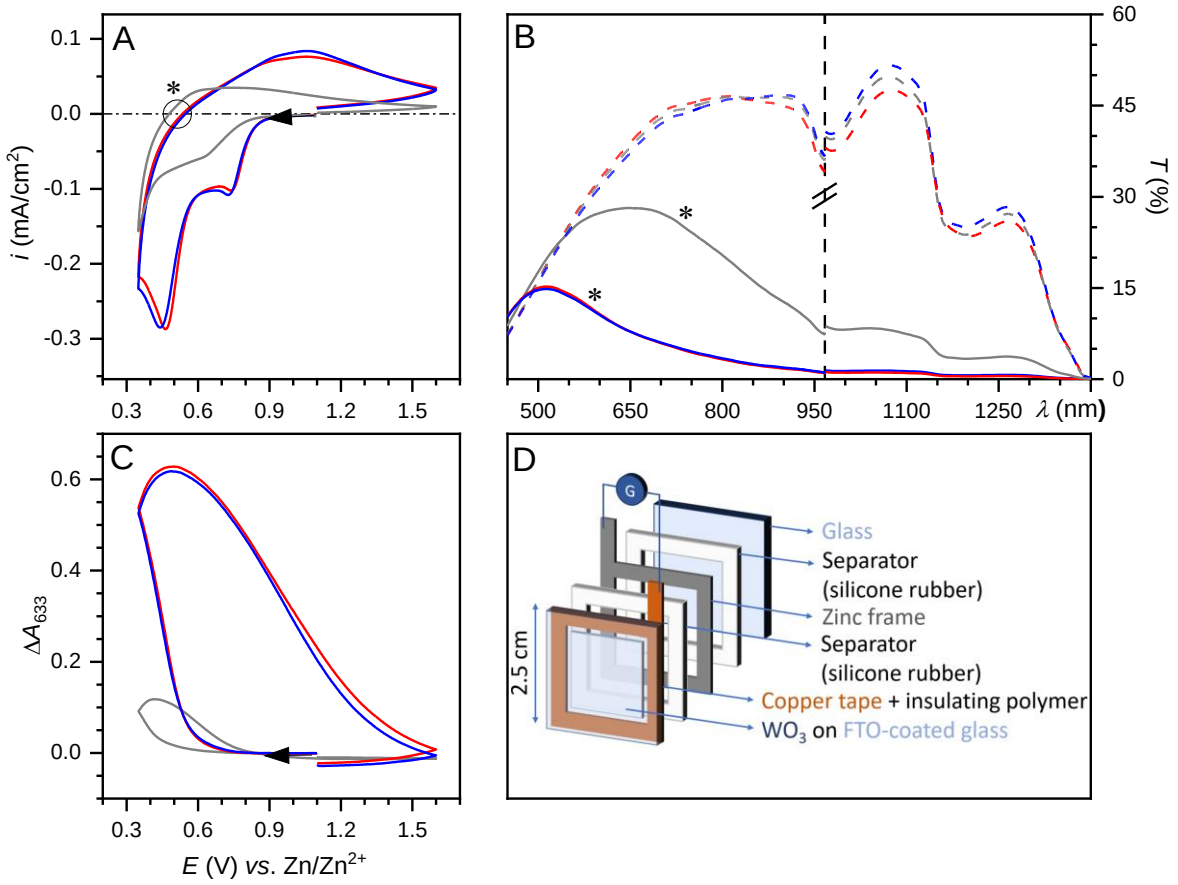

Figure 4. (A) CVs recorded at 5 mV/s for the Zn/WO_3 electrochromic device filled with the following different electrolytes (all at pH 3): (red) 0.1 M $ZnCl_2$ + 0.25 M $AlCl_3$, (blue) 0.1 M $ZnCl_2$ + 0.25 M CH_3COOH + 0.5 M KCl, and (grey) 0.1 M $ZnCl_2$ + 1 M KCl. (B) Simultaneously recorded transmittance spectra of the WO_3 electrochromic device over the 450-1350 nm wavelength range (same colour code as in A) for (dashed lines) the initial discharged state and (plain lines) fully charged state (corresponding to * in A). (C) CVAs of the WO_3 electrochromic device at 633 nm (same colour code as in A). (D) Split view of the Zn/WO_3 electrochromic device.

The CVs recorded for the Zn/WO_3 electrochromic device in $ZnCl_2$ electrolytes supplemented with $AlCl_3$ or acetic acid overlap perfectly. They both present two well-defined reduction peaks and a single broader reoxidation peak, a shape very similar to those reported in Figure 3A. This thus indicates that an identical electrochemical proton insertion mechanism is at work at the WO_3 electrode and so that the presence of $ZnCl_2$ does not significantly interfere with or affect this mechanism. Consequently, in the presence of $AlCl_3$ or acetic acid, the following comprehensive reaction can be proposed to interpret the reversible colouring/bleaching process of the device (see also Figure S3 for the operating principle):

$$WO_3 + x\,AH + \frac{x}{2}\,Zn^{2+} \rightleftarrows H_xWO_3 + x\,A^- + \frac{x}{2}\,Zn \qquad (5)$$

Concerning the spectral characteristics of the device, it can be seen that the transmittance of the smart window is the same for the electrolyte containing $AlCl_3$ or acetic acid, whatever the state of

charge, as evidenced by the overlap of transmittance spectra over the entire wavelength range from 450 to 1350 nm (Figure 4B). The same conclusion can be inferred from the cyclic voltabsorptograms (CVA) monitored at 633 nm (Figure 4C). It is interesting to note that the coloration of WO_3 is mainly linked to the second faradaic process, insofar as the absorbance variation develops mainly at potentials below 0.5 V (*vs*. Zn/Zn^{2+}). The lack of significant electrochromic properties during the first reduction peak is fully consistent with what was reported by Darmawi *et al.* for nanocrystalline WO_3 films in a 0.1 M H_2SO_4.[13]

In order to confirm the minor contribution of Zn^{2+} in the charge storage mechanism, the experiments were repeated with an aqueous electrolyte of pH 3 containing only 0.1 M $ZnCl_2$ along with 1 M KCl. The corresponding CV and CVA are shown in grey in Figures 4A and 4C. The CV reveals only one reduction peak, of very low magnitude and shifted significantly to negative potentials compared with those previously recorded in electrolytes containing acetic acid or $AlCl_3$. In addition, the overall charge passed and the reversible increase in absorbance at 633 nm remain very low. These observations clearly demonstrate the crucial role played by weak acids such as $[Al(H_2O)_6]^{3+}$ or acetic acid in facilitating proton insertion into WO_3, since, in their absence, Zn^{2+} makes only a minor contribution to the charge storage, whether as a multivalent insertion cation or as a weak Brønsted acid in its $[Zn(H_2O)_6]^{2+}$ form. The weak contribution of $[Zn(H_2O)_6]^{2+}$ as a proton donor can be explained by its much lower acidity (pK_a of 9.0)[33] as compared to $[Al(H_2O)_6]^{3+}$ (pK_a of 5.0). Furthermore, its contribution as a proton donor is expected to lead in a local pH increase, and thus a shift of the proton insertion potential towards more negative values, as has been reported for MnO_2 electrodes.[47] Therefore, the small amount of charge that reversibly accumulates here at the WO_3 cathode in the $ZnCl_2$ electrolyte, is most likely related to reversible insertion of protons supplied by $[Zn(H_2O)_6]^{2+}$ rather than reversible insertion of Zn^{2+} ions, as has been proposed in some studies.[6,30,48]

To assess the coloration efficiency of the Zn/WO_3 smart window, potential step chronoamperometric experiments were performed. To this end, the initially transparent smart window was subjected to a first potential step at 0.35 V during 20 s, followed then by a second potential step at 1.6 V for 100 s. Here again, the behaviour of devices containing $AlCl_3$ or acetic acid in the presence of $ZnCl_2$ are almost indistinguishable. During the first potential step, the transmittance of the devices decreases rapidly (Figure 5A) concomitantly with the appearance of a blue coloration at the cathode, as shown in Figure 5D (right picture). The process then inverts with the reversal of the potential step. However, bleaching turns out to be much slower, slowing down rapidly below < 2 mA/cm^2 (Figure 5C) despite the high voltage applied. This observation is in line with the cyclic voltammetric experiments discussed above, indicating a slow reoxidation of WO_3.

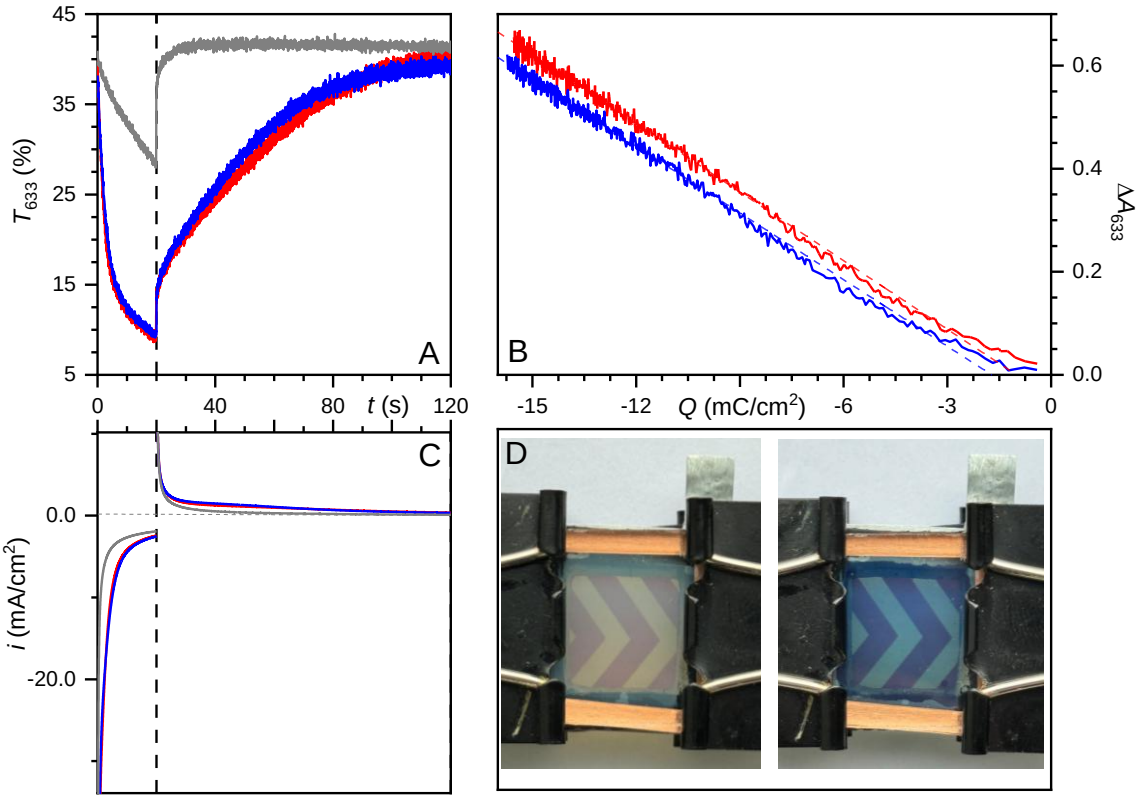

Figure 5. (A) Transmittance monitored at 633 nm at the Zn/WO_3 electrochromic device during colouring and bleaching chronoamperometric experiments in various electrolytes of pH 3 containing 0.1 M $ZnCl_2$ and (red) 0.25 M $AlCl_3$, (blue) 0.25 M acetic acid, (grey) 1 M KCl. (B) Variation of the absorbance at 633 nm as a function of the charge passed upon colouring (*i.e.*, WO_3 reduction). (C) Charge accumulated in the Zn/WO_3 device upon colouring and bleaching. (D) Pictures of the electrochromic device for different state-of-charge: (left) initial transparent state and (left) after 20 s at 0.35 V.

From the chronoamperometric experiments, the coloration efficiency η (in cm^2/C) at 633 nm of each device can be determined according to the following relationship:

$$\eta = \frac{d(OD)}{dQ} \qquad (6)$$

where *OD* is the optical density at a selected wavelength and *Q* (in C/cm^2) the charge injected.

Here, the coloration efficiency of the WO_3 thin film was deduced from the slope of the linear regression fit to the experimental data shown in Figure 5B (see dashed lines) over a 15 mC/cm^2 charge (equivalent to 42 mA·h/cm^2), leading to almost identical values of η_{633} = 43.1 and 44.4 ± 0.2 cm^2/C in the presence of acetic acid and $AlCl_3$, respectively. Such level of charge/coloration is associated to a light blue coloration of the device (Figure 5D), but full opacification could be reached upon longer polarization at low potentials and a total amount of charge of 40 mC/cm^2 (Figure S4). The coloration efficiency values reported here are very close to those reported for other Zn-based smart window device operating with dual Zn^{2+}/Al^{3+} electrolytes and incorporating either a WO_3

electrode prepared by electrodeposition (η_{633} = 54 cm^2/C)[48] or a $Nb_{18}W_{16}O_{93}$ cathode (η_{633} = 45.28 cm^2/C).[29] They are also similar to the value reported for the self-driven coloration of a sputtered WO_x film in a Cu-based smart window containing an $AlCl_3$ aqueous electrolyte (η_{633} = 36 cm^2/C).[49] However, in all these devices, the charge storage mechanism at the electrochromic cathode was attributed to the reversible insertion of Al^{3+}, while here we unambiguously demonstrate that it relies on PICET.

Conclusion

In the present study, by comparing the electrochemical reactivity of nanostructured γ-WO_3 electrodes in aqueous electrolytes of different chemical composition and pH, we demonstrate that reversible proton insertion is the sole charge storage mechanism at work in electrolytes containing a strong or weak Brønsted acid. We also reveal that the electrochemical behaviour of the electrode depends solely on the pH of the electrolyte, but not on the charge or chemical nature of the weak Brønsted acid, and this over a wide pH range. We furthermore provide evidence that this reversible proton insertion mechanism remains at work in electrolytes containing a multivalent cation such as Al^{3+}, as well as in electrolytes containing a mixture of two multivalent cations such as the Al^{3+}/Zn^{2+}-based electrolytes recently used in the development of Zn-based energy-saving smart windows. This new knowledge paves the way for the rational development of optimized mild-aqueous WO_3-based functional devices.

Experimental section

Chemicals and materials. All chemicals were provided by Sigma-Aldrich and used without further purification. All aqueous solutions were prepared using highly purified Milli-Q water (18.2 MΩ.cm). Zinc (99.5 %) metallic sheet of 0.25 mm thickness was brought from Goodfellow. Glass-FTO electrodes (7-10 Ω/□) were purchased from Solems. Conductive Copper tape (3M) and Silicone rubber sheet (1.5 mm thick) were purchased from RS Components.

Preparation of the tungsten oxide electrodes. The porous and nanostructured WO_3 electrodes were prepared by hydrothermal synthesis on transparent conducting commercially available substrates made of a glass sheet coated with a fluorine-doped tin oxide (FTO) conducting film. The substrates were washed successively with Milli-Q water, ethanol, and acetone for 5 minutes in an ultrasonic bath, followed by 2 hrs calcination at 500°C (ramp: 5°C/min) to remove any trace of organic pollution. A small surface is then covered with a silicone sheet to maintain a deposit-free zone for subsequent electrical contact. The substrates are subsequently plunged in the deposition solution (see below) and placed almost vertically into an autoclave, with the ITO film against the wall. The

deposition solution is prepared as follows: first, 1.25 g of tungstic acid (H_2WO_4, 99%) are dissolved in 30 mL of Milli-Q water and 10 mL of 30 wt % hydrogen peroxide (H_2O_2) and kept under stirring at 95°C for 30 minutes until discoloration. Next, the volume of the solution is adjusted to 100 mL by addition of 60 mL of Milli-Q water. Then, 6 mL of this previous solution are added in an acidic solution containing 1 mL of hydrochloric acid at 6 M, 5 mL Milli-Q water and 20 mL acetonitrile and the mixture is stirred for 5 min before to be placed within a 120 mL Teflon-lined stainless-steel autoclave. Finally, the autoclave was placed in a heat chamber at 180°C for 6 hours. The electrodes were then picked-up and calcinated at 600°C for an hour with a 3°C increase per minute ramp (after removal of the silicone mask) to allow the deposited film to crystallize in a monoclinic γ-WO_3 system.

Electrolytes. The electrolytes were all prepared in a 100 mL volumetric flask. The acetate buffer (0.5 M, pH 4.6) along with 0.5 M KCl was prepared from 1.43 mL of acetic acid (≥ 99%), 2.46 g of potassium acetate (≥ 99%) and 3.73 g of potassium chloride (≥ 99%). The phosphate buffer (0.5 M, pH 7) was prepared from 1.83 g of potassium phosphate dibasic (HK_2O_4P, ≥ 98%) and 3.00 g of potassium phosphate monobasic (H_2KO_4P, ≥ 99%). The ammonia buffer (0.5 M, pH 9.5) was prepared from 1.77 g of ammonium chloride (≥ 99%), 0.40 mL of ammonia (anhydrous, ≥ 99.9%). The potassium chloride electrolyte (1 M, pH 3) was prepared from 7.46 g of potassium chloride and acidified to pH 3 upon addition of few drops of a diluted HCl solution (0.37%). The aluminium chloride electrolyte (0.25 M Al^{3+}, pH 3) was prepared from 3.33 g of aluminium chloride (anhydrous, ≥ 99%). The acetic acid electrolyte (pH 3) containing 0.25 M acetic acid + 0.5 M KCl was prepared from 1.43 mL of acetic acid and 3.73 g of potassium chloride. The sulfuric acid electrolyte (0.1 M, pH 0.95) was prepared from 0.54 mL of sulfuric acid (95%). The Zn^{2+}-based electrolytes for the smart windows were prepared by adding 1.36 g of zinc chloride (anhydrous, ≥ 98%) to a 100 mL volumetric flask filled up with the appropriate electrolyte.

Electrochemical Characterization. Cyclic voltammetry and galvanostatic cycling experiments were performed using a BioLogic VSP potentiostat controlled by the EC-Lab software. In the standard three-electrode cell configuration, the counter electrode was a platinum wire, and the reference electrode was an Ag/AgCl/KCl_{sat} electrode (WPI, DriRef). Prior to measurements, the electrolyte (~20 mL) was carefully degassed (argon bubbling) for 20 min, and a constant argon flow was maintained above the electrochemical cell during the entire experiment. The current density was calculated from the current intensity normalized to the electrode geometric surface area.

Spectroelectrochemical Characterization. The visible-NIR transmittance spectra were recorded over 420-1700 nm using a bifurcated visible-NIR optical fiber connected to an HR-2000+ spectrometer (Ocean Optics) and a Flame-NIR spectrometer (Ocean Insight), both controlled by Ocean View software. The integration times were set at 30 ms and 1 ms for the HR-2000+ and FlameNIR

spectrometers, respectively, with an average of 30 and 100 scans, respectively. Light was provided by a DH-2000-BAL halogen lamp (Ocean Insight). All blank spectra were recorded in air.

Smart window assembly. The spectroelectrochemical measurements were performed at a Zn/WO_3-FTO smart window assembly. For such purpose, WO_3 was deposited onto a 2.5 × 2.5 cm^2 FTO electrode, using silicone rubber to mask ~2.5 mm wide areas around each edge. After removing of the silicone rubber and electrode calcination, a conductive copper tape was applied to the outer edges of the transparent electrodes to improve electrical connectivity, and subsequently covered with an insulating layer. This electrode was then combined to a silicone polymer frame as first separator, a Zn metal frame as the counter electrode, a second silicone polymer frame as second separator, and a microscope slide as back window. The smart window was sealed with clips and filled with ~1.2 mL of a degassed electrolyte.

Structural characterization. X-ray powder diffraction (XRD) measurements were carried out with a Panalytical X'pert Pro X-ray diffractometer equipped with a Co tube and an X'celerator detector. The 2θ range for each sample was from 10 to 100° with a step size of 0.08°. The collected data were carefully analyzed using HighScore$^+$ software. Scanning electron microscopy (SEM) was used to investigate the morphology of the electrodes and the size of WO_3 crystallites. An ultrahigh-resolution SUPRA 40 SEM (Zeiss) was used with a 5 kV accelerating voltage. X-ray photoelectron spectroscopy (XPS) analyses were performed on a K Alpha+ spectrometer (ThermoFisher), equipped with a monochromated X-Ray Source (Al Kα, 1486.6 eV).

Raman Spectroscopy. Raman spectra were recorded with a Labram microscope (Horiba Jobin-Yvon) equipped with a 100× objective and a 633 nm excitation wavelength. The spectra are the average of 3 individual spectra each recorded with a 5 s exposure time.

Supporting Information

Figure S1 to S4 : Cyclic voltammograms of the WO_3 electrode in the 0.5 M acetate buffer electrolyte at different scan rates ; Schematic view of the Zn/WO_3 smart window assembly ; Data and photograph of the Zn/WO_3 device charged up to 40 mC/cm^2.

References

[1] C. C. Mardare, A. W. Hassel, *Phys. Status Solidi A* **2019**, *216*, 1900047.
[2] S. K. Deb, *Sol. Energy Mater. Sol. Cells* **2008**, *92*, 245.
[3] C. G. Granqvist, M. A. Arvizu, Bayrak Pehlivan, H. Y. Qu, R. T. Wen, G. A. Niklasson, *Electrochimica Acta* **2018**, *259*, 1170.
[4] P. A. Shinde, S. C. Jun, *ChemSusChem* **2020**, *13*, 11.
[5] L. Shen, L. Du, S. Tan, Z. Zang, C. Zhao, W. Mai, *Chem Commun* **2016**, *52*, 6296.
[6] H. Li, C. J. Firby, A. Y. Elezzabi, *Joule* **2019**, *3*, 2268.
[7] Y. Shi, M. Sun, Y. Zhang, J. Cui, Y. Wang, X. Shu, *Sol. Energy Mater. Sol. Cells* **2020**, *212*, 110579.
[8] Y. Wang, W. Tian, C. Chen, W. Xu, L. Li, *Adv. Mater.* **2019**, *29*, 1809036.
[9] K. Machida, M. Enyo, *J. Electrochem. Soc.* **1990**, *137*, 1169.
[10] J. B. Mitchell, W. C. Lo, A. Genc, J. Lebeau, V. Augustyn, *Chem. Mater.* **2017**, *29*, 3928.
[11] H. Jiang, J. J. Hong, X. Wu, T. W. Surta, Y. Qi, S. Dong, Z. Li, D. P. Leonard, J. J. Holoubek, J. C. Wong, J. J. Razink, X. Zhang, X. Ji, *J. Am. Chem. Soc.* **2018**, *140*, 11556.
[12] C. Granqvist, In *Electrochromic Materials and Devices* (Eds.: Mortimer, R. J.; Rosseinsky, D. R.; Monk, P. M. S.), Wiley, **2013**, pp. 1–40.
[13] S. Darmawi, S. Burkhardt, T. Leichtweiss, D. A. Weber, S. Wenzel, J. Janek, *Phys Chem Chem Phys* **2015**, 15903.
[14] E. V Miu, J. R. McKone, G. Mpourmpakis, *J Am Chem Soc* **2022**, *144*, 6420.
[15] M. A. Spencer, J. Fortunato, V. Augustyn, *J Chem Phys* **2022**, *156*, 064704.
[16] A. Gorenstein, R. M. Torresi, M. V Vazquez, *J Electroanal Chem* **1991**, *318*, 131.
[17] A. Hu, Z. Jiang, C. Kuai, S. Mcguigan, D. Nordlund, Y. Liu, F. Lin, *J. Mater. Chem. A* **2020**, *8*, 20000.
[18] M. Anik, T. Cansizoglu, *J. Appl. Electrochem.* **2006**, *36*, 603.
[19] B. S. Lee, R. Deshpande, P. A. Parilla, K. M. Jones, B. To, A. H. Mahan, A. C. Dillon, *Adv. Mater.* **2006**, *18*, 763.
[20] Y. Tian, W. Zhang, S. Cong, Y. Zheng, F. Geng, Z. Zhao, *Adv. Funct. Mater.* **2015**, *25*, 5833.
[21] J. Zhao, Y. Tian, Z. Wang, S. Cong, D. Zhou, Q. Zhang, M. Yang, W. Zhang, F. Geng, Z. Zhao, *Angew. Chem. - Int. Ed.* **2016**, *55*, 7161.
[22] C. Chen, H. Zhu, M. Shi, L. Hu, Z. Xue, H. Ye, L. Zhao, C. Yan, *Energy Storage Mater.* **2022**, *49*, 370.
[23] J. Xie, B. Song, G. Zhao, G. Han, *Appl. Phys. Lett.* **2018**, *112*, 231902.
[24] H. Lahan, S. K. Das, *Dalton Trans.* **2019**, *48*, 6337.
[25] X. Huo, X. Miao, X. Han, S. Tang, M. Zhang, *J. Mater. Chem. A* **2020**, *8*, 9927.
[26] J. Guo, M. Wang, X. Diao, Z. Zhang, G. Dong, H. Yu, F. Liu, H. Wang, J. Liu, *J. Phys. Chem. C* **2018**, *122*, 19037.
[27] S. Sun, C. Tang, Y. Jiang, D. Wang, X. Chang, Y. Lei, N. Wang, Y. Zhu, *Sol. Energy Mater. Sol. Cells* **2020**, *207*, 110332.
[28] F. H. An, Y. Z. Yuan, J. Q. Liu, M. D. He, B. Zhang, *RSC Adv.* **2023**, *13*, 13177.
[29] C. Wu, H. Shi, L. Zhao, X. Chen, X. Zhang, C. Zhang, J. Yu, Y. Lv, R. Wei, T. Gao, J. Xie, Y. Yu, W. Liu, *Adv. Funct. Mater.* **2023**, *33*, 2214886.
[30] Q. Huang, S. Cao, Y. Liu, Y. Liang, J. Guo, R. Zeng, J. Zhao, B. Zou, *Sol. Energy Mater. Sol. Cells* **2021**, *220*, 110853.
[31] Z. Rong, R. Malik, P. Canepa, G. Sai Gautam, M. Liu, A. Jain, K. Persson, G. Ceder, *Chem. Mater.* **2015**, *27*, 6016.
[32] Y. Marcus, *J Chem Soc Faraday Trans* **1991**, *87*.
[33] S. J. Hawkes, *J. Chem. Educ.* **1996**, *73*, 516.

[34] Y.-S. Kim, K. D. Harris, B. Limoges, V. Balland, *Chem. Sci.* **2019**, *10*, 8752.
[35] V. Balland, M. Mateos, A. Singh, K. D. Harris, C. Laberty- Robert, B. Limoges, *Small* **2021**, *17*, 2101515.
[36] J. Guo, X. Guo, H. Sun, Y. Xie, X. Diao, M. Wang, X. Zeng, Z. Zhang, *ACS Appl. Mater. Interfaces* **2021**, *13*, 11067.
[37] M. J. Park, H. Yaghoobnejad Asl, A. Manthiram, *ACS Energy Lett.* **2020**, *5*, 2367.
[38] I. M. Szilágyi, B. Fórizs, O. Rosseler, Á. Szegedi, P. Németh, P. Király, G. Tárkányi, B. Vajna, K. Varga-Josepovits, K. László, A. L. Tóth, P. Baranyai, M. Leskelä, *J. Catal.* **2012**, *294*, 119.
[39] E. V Miu, J. R. McKone, *J. Mater. Chem. A* **2019**, *7*, 23756.
[40] G. Zhang, K. Guo, X. Shen, H. Ning, H. Liang, J. Zhong, W. Xu, B. Tang, R. Yao, J. Peng, *ACS Appl. Mater. Interfaces* **2021**, *13*, 4768.
[41] E. V. Miu, G. Mpourmpakis, J. R. McKone, *ACS Appl. Mater. Interfaces* **2020**, *12*, 44658.
[42] M. Rezrazi, B. Vuillemin, O. Bohnke, *J Electrochem Soc* **1991**, *138*, 2770.
[43] P. R. Smirnov, V. N. Trostin, *Russ. J. Gen. Chem.* **2013**, *83*, 15.
[44] W. M. Haynes, *CRC Handbook of Chemistry and Physics*, 95th Edition., CRC Press: Boca Raton, FL, **2014**.
[45] N. Makivić, K. D. Harris, J. Tarascon, B. Limoges, V. Balland, *Adv. Energy Mater.* **2023**, *13*, 2203122.
[46] L. E. Blanc, D. Kundu, L. F. Nazar, *Joule* **2020**, *4*, 771.
[47] M. Mateos, N. Makivic, Y. Kim, B. Limoges, V. Balland, *Adv. Energy Mater.* **2020**, *10*, 2000332.
[48] H. Eric, H. Li, E. Adulhakem Y., *RSC Adv.* **2019**, *9*, 32047.
[49] J. Guo, X. Diao, M. Wang, Z.-B. Zhang, Y. Xie, *ACS Appl. Mater. Interfaces* **2022**, *14*, 10517.

Supplementary Information to

Multivalent-ion versus proton insertion into nanostructured electrochromic WO_3 from mild aqueous electrolytes

T. Rocca[1], A. Gurel[2], D. Schaming[2], B. Limoges[1,*], V. Balland[1,*]

1- Université Paris Cité, Laboratoire d'Electrochimie Moléculaire, UMR 7591, 75006 Paris Cedex 05
2- Université Paris Cité, ITODYS, UMR 7086, 75006 Paris Cedex 05

Corresponding authors:

limoges@u-paris.fr

veronique.balland@u-paris.fr

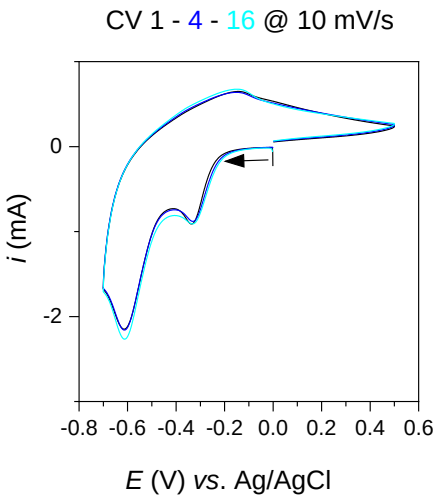

Figure S1. Cyclic voltammograms of the WO_3 electrode in the 0.5 M acetate buffer electrolyte at 10 mV/s. Black, blue and cyan curves correspond to cycle 1; 4 and 16 respectively.

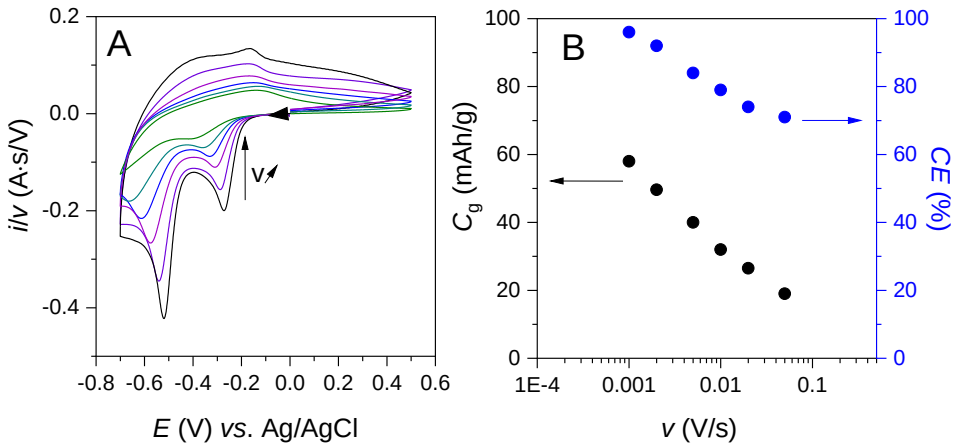

Figure S2. (A) Cyclic voltammograms of the WO_3 electrode in the 0.5 M acetate buffer electrolyte recorded from (black) 1 to (green) 50 mV/s, and (B) associated (black) gravimetric capacity and (blue) Columbic Efficiency as a function of the scan rate.

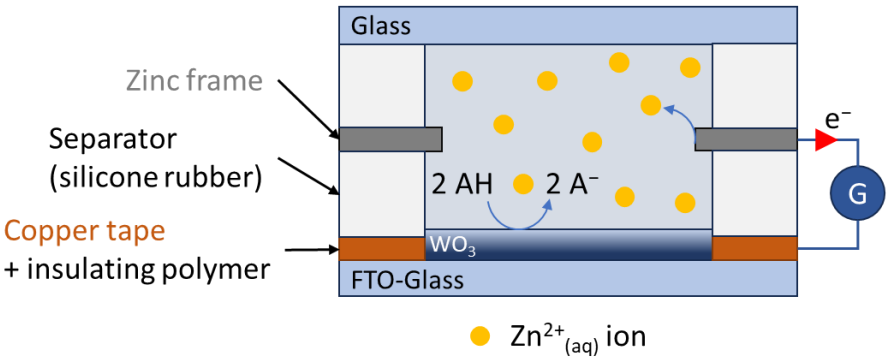

Figure S3. Sectional view of the Zn/WO_3 smart window assembly showing the device in operation (colouring/charging step).

At the anode: $WO_3 + x\ AH + \ x\ e^- \rightleftarrows \ H_xWO_3 + x\ A^-$

At the cathode: $Zn \ \rightleftarrows Zn^{2+} + 2e^-$

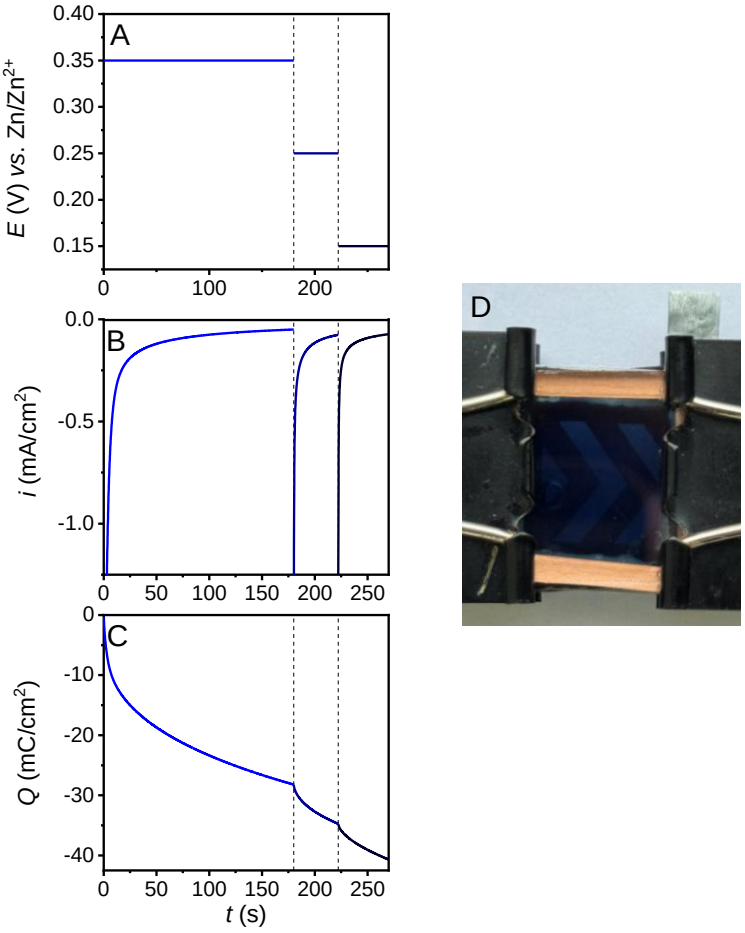

Figure S4. 2.5 x 2.5 cm^2 Zn/WO_3 device filled with the 0.1 M $ZnCl_2$ + 0.25 M CH_3COOH + 0.5 M KCl electrolyte (pH 3) and submitted to three successive potential steps at 0.35 V (for 180 s), next 0.25 V (for 42 s) and finally 0.15 V (for 48 s). (A) Applied potential; (B) current density and (C) charge passed as a function of time. (D) photograph in the fully charged state.